

Microstructure evolution and mechanical properties in a gas tungsten arc welded Fe₄₂Mn₂₈Co₁₀Cr₁₅Si₅ metastable high entropy alloy

Jiajia Shen ^{a, **}, Priyanka Agrawal ^{b,c}, Tiago A. Rodrigues ^a, J.G. Lopes ^a, N. Schell ^d, Jingjing He ^e, Zhi Zeng ^f, Rajiv S. Mishra ^{b,c}, J.P. Oliveira ^{a,g,*}

^a UNIDEMI, Department of Mechanical and Industrial Engineering, NOVA School of Science and Technology, Universidade NOVA de Lisboa, Caparica, 2829-516, Portugal

^b Center for Friction Stir Processing, Department of Materials Science and Engineering, University of North Texas, Denton, TX, 76207, USA

^c Advanced Materials and Manufacturing Processes Institute, University of North Texas, Denton, TX, 76207, USA

^d Institute of Materials Physics, Helmholtz-Zentrum Hereon, Max-Planck-Str. 1, Geesthacht, D-21502, Germany

^e School of Reliability and Systems Engineering, Beihang University, Beijing, 100191, China

^f School of Mechanical and Electrical Engineering, University of Electronic Science and Technology of China, Sichuan, 611731, China

^g CENIMAT/I3N, Department of Materials Science, NOVA School of Science and Technology, Universidade NOVA de Lisboa, 2829-516, Caparica, Portugal



ARTICLE INFO

Keywords:

Metastable high entropy alloys
Fe₄₂Mn₂₈Co₁₀Cr₁₅Si₅
Gas tungsten arc welding
Synchrotron X-ray diffraction
Thermodynamic calculations
Mechanical testing

ABSTRACT

Weldability studies on high entropy alloys are still relatively scarce, delaying the deployment of these materials into real-life applications. Thus, there is an urgent need for in-depth studies of the weldability of these novel advanced engineering alloys. In the current work, an as-cast Fe₄₂Mn₂₈Co₁₀Cr₁₅Si₅ metastable high entropy alloy was welded for the first time using gas tungsten arc welding. The weld thermal cycle effect on the microstructure evolution over the welded joint was examined using electron microscopy in combination with electron back-scatter diffraction, synchrotron X-ray diffraction analysis, and thermodynamic calculations. Furthermore, tensile testing and hardness mapping were correlated with the microstructure evolution. The microstructure evolution across the joint is unveiled, including the origin of the ε-h.c.p. phase at different locations of the material. Different strengthening effects measured throughout the joint are associated with the weld thermal cycle and resulting microstructure. A synergistic effect of smaller grain size of the ε-h.c.p. phase in the fusion zone, overturns the reduced volume fraction of this phase, increasing the local strength of the material. Moreover, the brittle nanosized σ phase was also found to play a critical role in the joints' premature failure during mechanical testing.

1. Introduction

High entropy alloys (HEAs) are a new class of materials that have emerged in recent years. This group of materials consist of at least five principal elements, and the concentration of each element typically varies from 5 to 35 at. % [1]. Four distinct core effects are conferred on these materials by this unique design concept, specifically, the lattice distortion effect [2], the high entropy effect [3], the cocktail effect [4] and the sluggish diffusion effect [5]. The four core effects associated to HEAs act as the main drivers for their development as they provide unique metallurgical properties, such as the ability to be ductile yet strong [6], thermally stable [7,8], corrosion resistant [9,10], and have

excellent mechanical properties both at high and low temperatures [11].

Extensive literature [12,13] shows that the most widely studied HEA, the equiatomic and f.c.c. single phase CoCrFeMnNi alloy, possesses high ductility, but relatively low mechanical strength which prevents its use in several practical applications. Recent developments in the field of non-equiatomic HEAs with tunable phase stability have led to breaking the strength-plasticity barrier by triggering twinning-induced plasticity (TWIP) and transformation-induced plasticity (TRIP) effects simultaneously, improving both strength and ductility [14]. Based on this design concept, Nene et al. [15] examined the impact of Si addition to the Fe–Mn–Co–Cr system on the metastability of the γ-f.c.c. phase, showing that the addition of 5 at. % Si was able to achieve a maximum

* Corresponding author. CENIMAT/I3N, Department of Materials Science, NOVA School of Science and Technology, Universidade NOVA de Lisboa, 2829-516, Caparica, Portugal.

** Corresponding author.

E-mail addresses: j.shen@campus.fct.unl.pt (J. Shen), jp.oliveira@fct.unl.pt (J.P. Oliveira).

metastability of the γ -f.c.c. phase. This allowed to develop an alloy with an optimized metastable microstructure with a composition of $\text{Fe}_{42}\text{Mn}_{28}\text{Co}_{10}\text{Cr}_{15}\text{Si}_5$ (at. %).

Welding is one of the most effective metal processing methods that is utilized in a wide range of industrial applications when it comes to structural engineering, including automobile, aerospace, and marine industries. During any welding process, the weld thermal cycle is of paramount importance to control both the solidification conditions and the potential solid-state transformations that may occur upon cooling from high temperature regimes in the heat affected and fusion zones. Specifically, for arc-based welding the welding current, I , voltage, V , and travel speed, v , of the heat source, as well as, the process efficiency, η , are the main parameters determining the heat input, HI , that is provided to the material to be welded. Here, it is worth mention that the energy efficiency for arc-based welding is relatively low, around 30–50% depending on the specific welding process. The heat input is a fundamental parameter during fusion welding, and is defined as $HI = \eta P/v$, where P is the power ($I \times V$). Usually, a decrease in heat input is targeted, since the larger the heat input the larger the extension of the thermally affected regions (fusion and heat affected zones) and the potential microstructure changes induced by the weld thermal cycle can be more notorious. Intimately related to the heat input is the cooling rate, where higher values of heat input led to lower cooling rates across the welded joint. Thus, proper selection of the heat input during fusion-based welding is important to control the microstructure evolution as well as the magnitude of residual stresses.

The excellent properties of HEAs make them suitable for a wide range of applications. Potential applications include moulds and tools, engines, wear-resistant coatings, nuclear applications, thermal barriers and corrosion-resistant applications as in the oil & gas industry, for example. Any of these applications eventually requires welding, thus the need to explore the weldability of HEA with potential application prospects. Considering the relevance of HEAs as potential structural engineering materials, welding will become increasingly necessary to construct complex shaped structures or to combine their properties with those of other materials. Therefore, to ensure the feasibility of using these new advanced alloys in real-life applications, their weldability needs to be addressed.

Up to now, most studies on TWIP/TRIP metastable HEAs have primarily focused on their thermo-mechanical processing, phase formation characterization, assessment of mechanical properties, as well as physical and chemical performances [6,16–19]. Weldability of TWIP/TRIP metastable HEAs has been addressed in only two reports, both using friction stir welding [20,21]. Thus, weldability studies for metastable HEAs considering fusion-based welding methods have not yet been reported.

The work presented here is the first to use gas tungsten arc welding to weld an as-cast TWIP/TRIP $\text{Fe}_{42}\text{Mn}_{28}\text{Co}_{10}\text{Cr}_{15}\text{Si}_5$ metastable HEA for the purpose of obtaining and discussing new data for the widespread applications of these advanced engineering alloys. To determine how the weld thermal cycle affects the evolution of microstructure across the entire joint, a combination of electron microscopy, high-energy synchrotron X-ray diffraction analysis and thermodynamic calculations were used. In addition, further clarification of the processing/microstructure/properties relationships was achieved by using tensile testing and microhardness mapping. Through multiscale and comprehensive characterizations of these novel materials, a deeper understanding of the correlation between processing, microstructure, and mechanical properties is gained paving the way for their wide application in a variety of fields.

Table 1
Welding parameters for the $\text{Fe}_{42}\text{Mn}_{28}\text{Co}_{10}\text{Cr}_{15}\text{Si}_5$ HEA.

Current (A)	Voltage (V)	Welding speed (mm/ min)	Shielding gas	Gas flow rate (L/ min)	Heat input (J/ mm)
25	8	150	99%	14	80

2. Experimental procedure

2.1. Starting material

The material used in this work was an as-cast non-equiautomic metastable $\text{Fe}_{42}\text{Mn}_{28}\text{Co}_{10}\text{Cr}_{15}\text{Si}_5$ (at. %) HEA, which was produced at Sophisticated Alloys Inc. in Butler, PA, USA, by vacuum induced melting in an argon atmosphere [22]. Prior to welding, sheets with a thickness of 1.5 mm were cut into $80 \times 40 \text{ mm}^2$ parts. Afterwards, the welding specimens were cleaned with acetone and ethanol to ensure that there were no potential contaminations on the joining surfaces.

2.2. Gas tungsten arc welding

To study the weldability of the as-cast $\text{Fe}_{42}\text{Mn}_{28}\text{Co}_{10}\text{Cr}_{15}\text{Si}_5$, gas tungsten arc welding was used. Here, 99.99% Ar as a shielding gas was used at a flow rate of 14 L/min. To prevent contamination on both sides (face and root) of the weld, as well as for minimizing the oxidation of the heat affected zone, the shielding gas was injected at both surfaces of the weld. The selected welding parameters are listed in Table 1. After welding, dog-bone shaped specimens were cut from the as-welded samples using electrical discharge machining (EDM) for subsequent microstructure and mechanical characterization.

2.3. Microstructure characterization

Prior to metallographic observations, the welded joints were mounted in epoxy resin, polished with 400–4000 grit SiC papers, and a final polishing step was conducted with diamond suspension of 3 μm . After being ground and polished, the microstructure of the joint was revealed with Keller's reagent, which was composed of 5 g CuCl_2 , 5 g HCl, 100 ml $\text{C}_2\text{H}_5\text{OH}$. The holding time for etching the material was approximately 90 s. An inverted optical microscope (OM) (Leica DMI 5000 M), a scanning electron microscope (SEM) (Helios Hikari UMSII) equipped with energy dispersive spectroscopy (EDS), and a field emission SEM (JSM-7100F) were used for metallographic observations. The raw EBSD data were post-processed using the orientation imaging microscopy analysis program (TSL OIM Analysis 7.2), and eventually the Kernel average misorientation (KAM), grain size and inverse pole figure (IPF) maps were extracted.

To determine the existing phases and evolution of phase fractions across the joints, synchrotron X-ray diffraction was employed. Experiments were conducted at PETRA III of DESY (Hamburg, Germany) using the P07 Energy Materials Science beamline. An 87 kV ($\lambda = 0.14235 \text{ \AA}$) monochromatic beam energy was used and the beam size was $200 \mu\text{m} \times 200 \mu\text{m}$. The measurements, performed in transmission mode, initially started from the base material, then travel through the heat affected zone as well as the fusion zone, and eventually ended on the opposite side of the base material with incremental steps of 200 μm . A two-dimensional PerkinElmer detector with pixel size of $200 \times 200 \mu\text{m}^2$ was used to acquire the Debye-Scherrer diffraction rings. The setup used is shown in Fig. 1. After the collection of the 2D images, a combination of Fit2D and Rietveld refinement using MAUD software were applied to post-process the raw data.

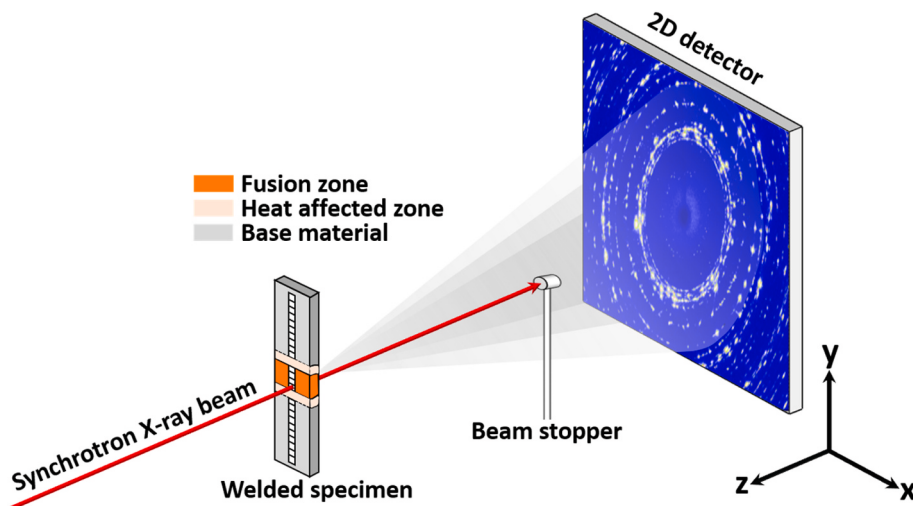


Fig. 1. Synchrotron X-ray diffraction setup (not to scale).

2.4. Thermodynamic calculations

For thermodynamic analysis, ThermoCalc software [23] was used with the latest TCHEA5.1 database for HEAs. Here, considering the non-equilibrium solidification that occurs in the fusion zone under the rapid cooling condition, the Scheil-Gulliver model [24] was employed to predict the solidification path and the potential phase formation in this region. For these calculations, both the nominal composition of the base material, as well as the measured average fusion zone composition were considered to evaluate potential changes in the solidification pathway of the material. The composition of the phases that were expected to be formed according to the Scheil-Gulliver model were also obtained and compared to those measured by SEM/EDS.

2.5. Microhardness and mechanical testing

To explore how the weld thermal cycle affect the hardness behavior over the welded joint, a Micro-Vickers Hardness testing machine, Mitutoyo HM-112, was used to measure the microhardness over the welded joint with a load of 0.3 kg over a 10s time period. A bidimensional map covering the entire cross-section enabled to evaluate strengthening and softening effects induced by changes in the microstructure as a result of the welding procedure. Besides, the mechanical response of the welded joints have also been further studied by conducting tensile tests. Dog-bone shaped specimens of the welded joints were obtained by EDM with 25.72 mm in gauge length, 1.5 mm in width and 1.5 mm in thickness, which were then deformed at room temperature by using a Shimadzu tensile machine under a strain rate of $1 \times 10^{-3} \text{ s}^{-1}$. Upon fracture of the welded joints, the fracture mechanism was determined using a Hitachi SU3800 SEM.

3. Results and discussion

3.1. Microstructure evolution

Fig. 2 a) provides a cross-sectional view of the as-cast Fe₄₂Mn₂₈Co₁₀Cr₁₅Si₅ gas tungsten arc welded joint. There, it can be observed that the welding parameters that were selected enabled a full penetration joint to be formed. A closer inspection of the cross section shows that there are no visible defects, such as pores or cracks. To clearly image representative microstructural features, optical microscopy images of the base material, heat affected zone, boundary between the heat affected zone and fusion zone, as well as the fusion zone are detailed in Fig. 2 b1), b2), b3) and b4), respectively. Based on the distinct boundaries that appear in the micrograph after etching, complete grains can be

identified as marked by dashed yellow lines, as shown in Fig. 2 b1, b2) and b4). The bright and dark contrasting colors are related to the microstructural features of both phases, corresponding to the γ -f.c.c. and ϵ -h.c.p. phase, respectively. Besides, scans of the same regions taken at high magnifications using electron microscopy are shown in Fig. 2 c1), c2), c3) and c4), respectively. The boundaries of the fusion zone are indicated by red dashed lines, as shown in Fig. 2 a).

Overall, a dual γ -f.c.c./ ϵ -h.c.p. microstructure is evidenced across the welded joint. The bright and dark contrasting colors are related to the microstructural features of both phases. A further detailed description will follow with respect to the microstructure that exists over the four typical regions of a welded joint, beginning with the so-called base material. This region mainly consists of two phases: a γ -f.c.c. matrix phase and ϵ -h.c.p. phase. In the γ -f.c.c. matrix phase, the ϵ -h.c.p. phase forms within it and mainly exhibits a block-shaped morphology [25], as indicated by the red arrows in Fig. 2 b1). Here, it is important to mention that the initial ϵ -h.c.p. phase formed was thermally induced upon cooling from the casting process used to obtain the starting base material. Entering in the heat affected zone (refer to Fig. 2 b2)), the microstructure is found to retain the dual γ -f.c.c./ ϵ -h.c.p. phase structure, with the parent γ -f.c.c. phase appearing to be partitioned by laths of ϵ -h.c.p. phase that cross-cut individual grains, and filled with compact laths, as marked by the white solid line in Fig. 2 b2).

Ahmed et al. [26] previously provided an interesting insight on how the interlath spacing (i.e., the distance between ϵ -h.c.p. laths) evolves. They conducted an examination of the ϵ -h.c.p. laths morphologies under different annealing conditions and found that the variations in the average interlath spacing is consistent with the trends in the ϵ -h.c.p. phase volume fraction, where the increased volume fraction of the ϵ -h.c.p. phase will lead to an increase in the density of ϵ -h.c.p. laths. This will be further discussed in the next section when evaluating the volume fraction changes across the welded joint. Moreover, from the base material (Fig. 2 b1)) to the heat affected zone (Fig. 2 b2)), a clear increase in grain size is evident as a result of the increased local peak temperature and permanence at high temperatures where solid-state phenomena, such as grain growth, can occur. This is a typical feature of fusion-based welding processes.

The heat affected zone/fusion zone boundary is clearly observed in Fig. 2 c3), because of the significant differences in the microstructure that exist in each region. These changes are attributed to the different weld thermal cycle experienced at each location, where the heat affected zone remains in the solid state, while in the fusion zone there is melting followed by solidification. Specifically, when weld solidification occurs, epitaxial nucleation is then triggered under the support of the cold heat affected zone, which serves as a substrate, and then grain growth ensues

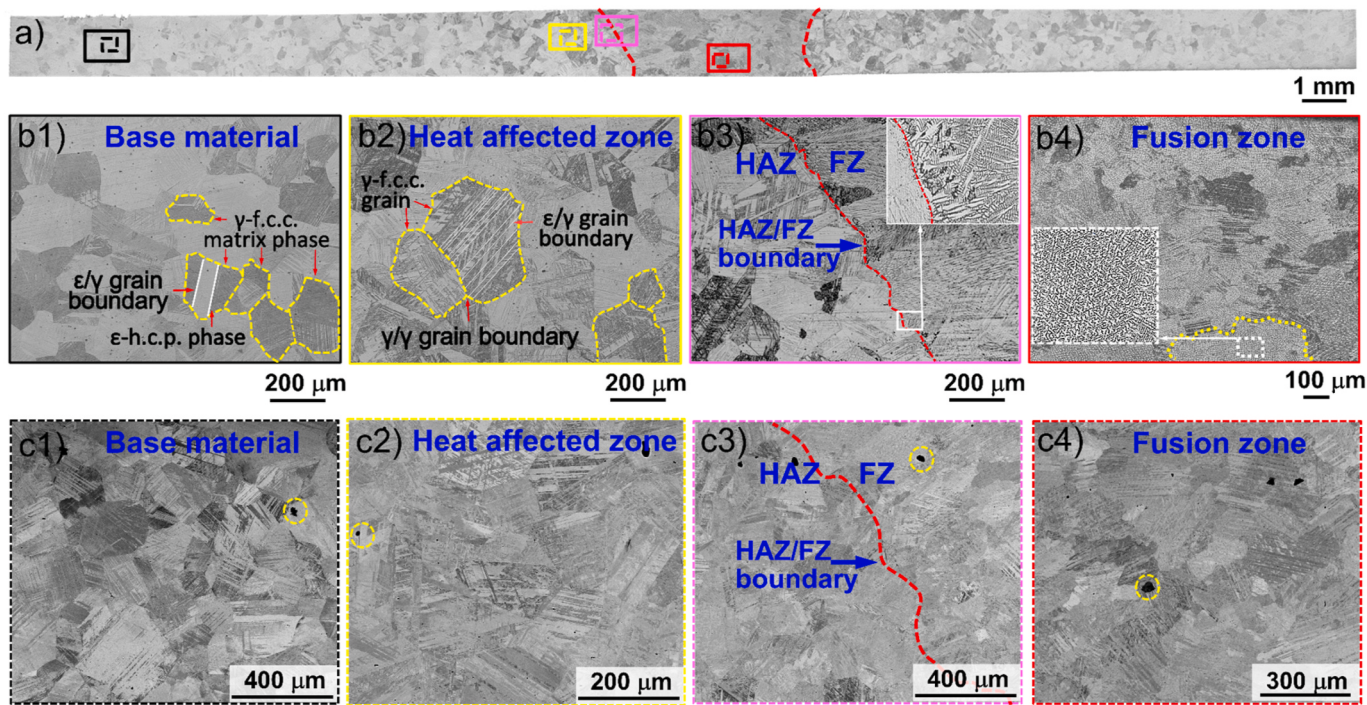


Fig. 2. a): a cross-sectional view of the welded joint; b1) and c1), b2) and c2), b3) and c3), c4) and d4) are close-up views of optical/electron microscopy for the base material (BM), heat affected zone (HAZ), boundary of heat affected zone and fusion zone (HAZ/FZ), and fusion zone (FZ), respectively.

in accordance with the direction of the maximum temperature gradient in the fusion zone. Here, at the edge of the fusion zone, a fine dendritic structure is observed as a result of the fast cooling rate enabled by the previously cold heat affected zone. Then, grains will start to grow towards the weld centerline (refer to Fig. 2 c3) and associated insert), which is consistent with the solidification theory that is used during fusion-based welding processes [27]. While moving away from the heat affected zone/fusion zone boundary towards the weld centerline, the grain structure formed is mainly composed of finer equiaxed grains (refer to Fig. 2 b4) whose formation is controlled by the degree of constitutional undercooling, i.e., the ratio of the temperature gradient, G , to the solidification rate, R , with a low G/R ratio being beneficial in promoting the formation of equiaxed grains [28]. A grain is marked by the dashed yellow line inserted in Fig. 2 b4), where the white dashed box in the grain is marked for a magnified microstructure view. The Nano Measure 1.2 software was used to quantify the size of the subgrains and their average size was approximately 2 μm .

Interestingly, the four regions of the welded joint evidence, according to the high magnification electron microscopy images, minor black spots (marked by yellow dashed circles), and most of them are concentrated on the phase boundaries, resembling welding defects such as pores and voids. However, EDS measurements detail that these spots correspond to the presence of Si–Mn-rich σ phase. This identification is corroborated by both synchrotron X-ray diffraction measurements, as well as thermodynamic calculations all of which will be further discussed in subsequent sections.

Fig. 3 a) details the EBSD map of the gas tungsten arc welded Fe₄₂Mn₂₈Co₁₀Cr₅Si₅ joint. Owning to the large dimensions of the joint and symmetry along the weld centerline, as observed in the optical micrograph of Fig. 1 a), only half of the joint is shown. Here, the solid and dashed black lines on Fig. 3 a) represent the boundary lines of the heat affected zone/fusion zone, and the base material/heat affected zone, respectively. The former boundary line can be determined by the distinctive differences in microstructural features between the heat affected zone and fusion zone. While for the latter boundary line, there are two main criterions for distinguishing the microstructure of each region: one is the grain size variation of the matrix γ -f.c.c. (refer to Fig. 3

e.), while the other one is the hardness distribution in three typical regions (further detailed in Fig. 8), in which the numerical variation in the hardness distribution of the joints can help to identify the ranges for these three typical regions. In addition, the IPF, KAM and phase maps of the base material (corresponding to Fig. 3 b1), b2) and b3), respectively), heat affected zone (corresponding to Fig. 3 c1), c2) and c3), respectively) and fusion zone (corresponding to Fig. 3 d1), d2) and d3), respectively) are also shown. It is worth noting that due to the low resolution and magnification of the present EBSD scanning, as well as the limitation of the EBSD scanning area, to identify all the fine ϵ -h.c.p. martensite laths [29]. Thus, the EBSD phase maps data presented here are only used to qualitatively identify the microstructure features across the joint, as well as to perform a qualitative comparison of trends in the volume fraction of γ -f.c.c. and ϵ -h.c.p. phases rather than a quantitative analysis. Further quantitative assessment will be performed with the high energy synchrotron X-ray diffraction data.

In the fusion zone, large columnar grains are observed (refer to Fig. 3 a)), which results from grain growth starting on the pre-existing solid material, where a large thermal gradient exists promoting the formation of a fine grain structure at the edge of the fusion zone. As mentioned before, the growth of grains tends to follow a direction perpendicular to the solid-liquid interface, the direction of the maximum temperature gradient, and nucleation is preferentially initiated at the cold substrate, producing fine dendritic grains at that point, as previously shown in Fig. 2 b3). However, when the solidification proceeds toward the weld centerline, competitive growth between grains will induce certain specific orientations, where grain growth will be facilitated if they are aligned more favorably with the heat flow. Here, during the relatively rapid cooling of the fusion zone, the IPF map demonstrates that the preferential growth direction of the γ -f.c.c. and ϵ -h.c.p. phases, shown in Fig. 3 g1) and g2), is preferentially along the (001) and (0001) directions, respectively. This can be evaluated by the distribution of existing grains in the orientation triangle shown in Fig. 3 g1) and g2). These two directions are marked with a red ellipse detailing the higher fraction of grains oriented at or close to these directions. Both preferential growth directions of the γ -f.c.c. and ϵ -h.c.p. phases along the (001) and (0001) directions, respectively, are in line with the easy growth

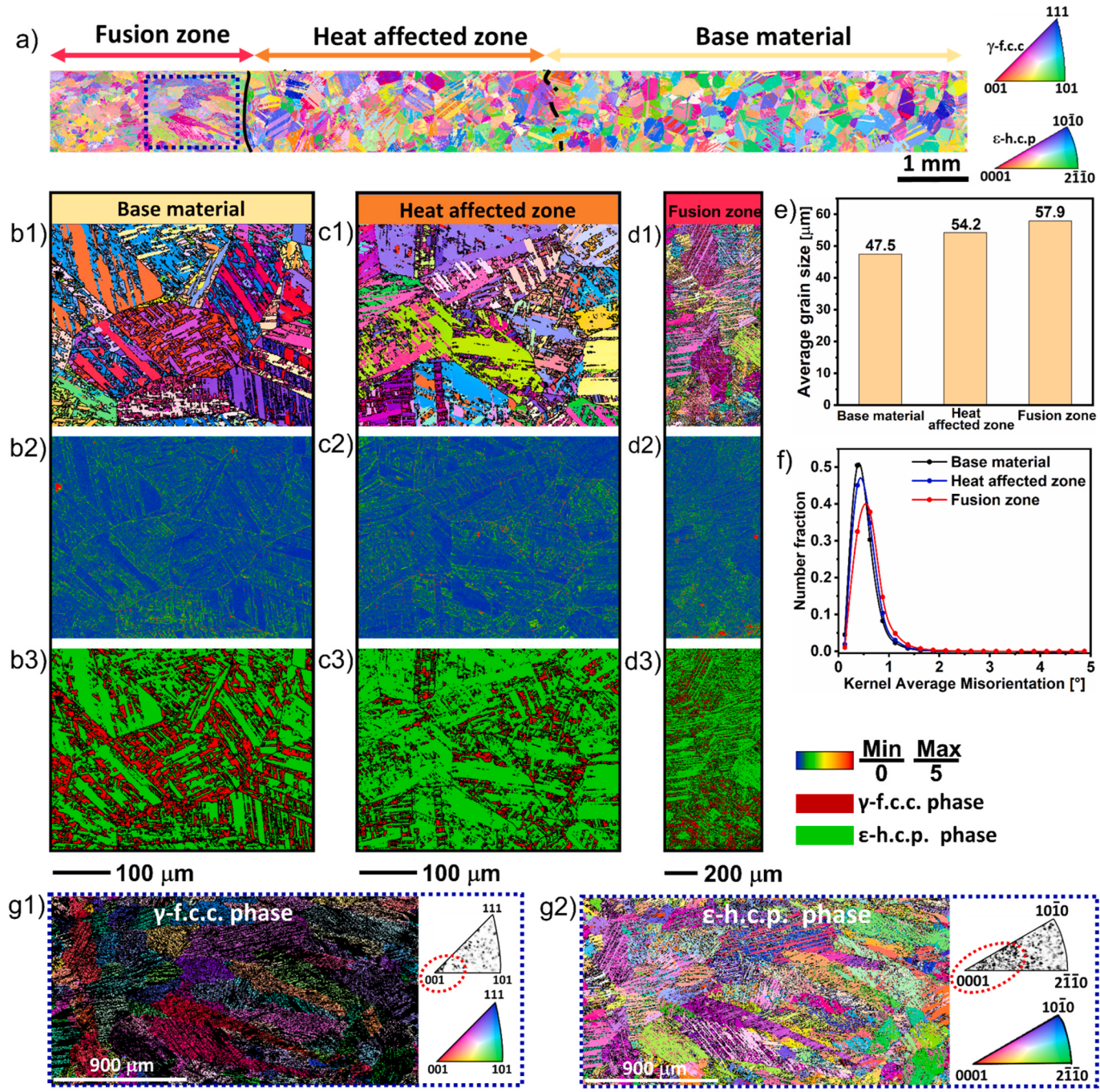


Fig. 3. a) EBSD map of the gas tungsten arc welded $\text{Fe}_{42}\text{Mn}_{28}\text{Co}_{10}\text{Cr}_{15}\text{Si}_5$ joint; b1) – b3): IPF map, KAM and phase map of the base material, respectively; c1) – c3): IPF map, KAM and phase map of the heat affected zone, respectively; d1) – d3): IPF map, KAM and phase map of the fusion zone, respectively; e) and f) variation of the average grain size and KAM values with respect to the different regions of the joint, respectively; g1) and g2) are the IPF of γ -f.c.c. and ϵ -h.c.p. phases, respectively.

directions for these crystal structures [30].

Fig. 3 b1), c1), and d1) illustrate the KAM maps of the base material, heat affected zone, and fusion zone, respectively. Generally, point to point measurements of local misorientation of grains in the surrounding microstructure define a KAM map. To further evaluate the variation of the KAM values across the welded joint, Fig. 3 f) details the average KAM values for different regions. Comparing the KAM maps (Fig. 3 b3), c3), and d3)) and values (Fig. 3 f)) in different regions, it is evident that the local deformation over the whole welded joint is quite low.

Based on the calculations made from multiple EBSD maps, Fig. 3 e)

provides the variation of the average grain size of the γ -f.c.c. phase in different regions of the welded joint. It should be noted that the values of the measured γ -f.c.c. grain size refers to the size of the whole matrix grains, which may contain the ϵ -h.c.p. laths. In the base material region, there is an average grain size of approximately $47.5 \mu\text{m}$. Then, the average grain size increases to around 54.2 and $57.9 \mu\text{m}$ when entering the heat affected zone and fusion zone, respectively. It is well known that the heat affected zone near the base material and heat affected zone near the fusion zone, are expected to exhibit different microstructure features owing to the differences in both peak temperature and permanence time at which solid-state transformations can occur. Although

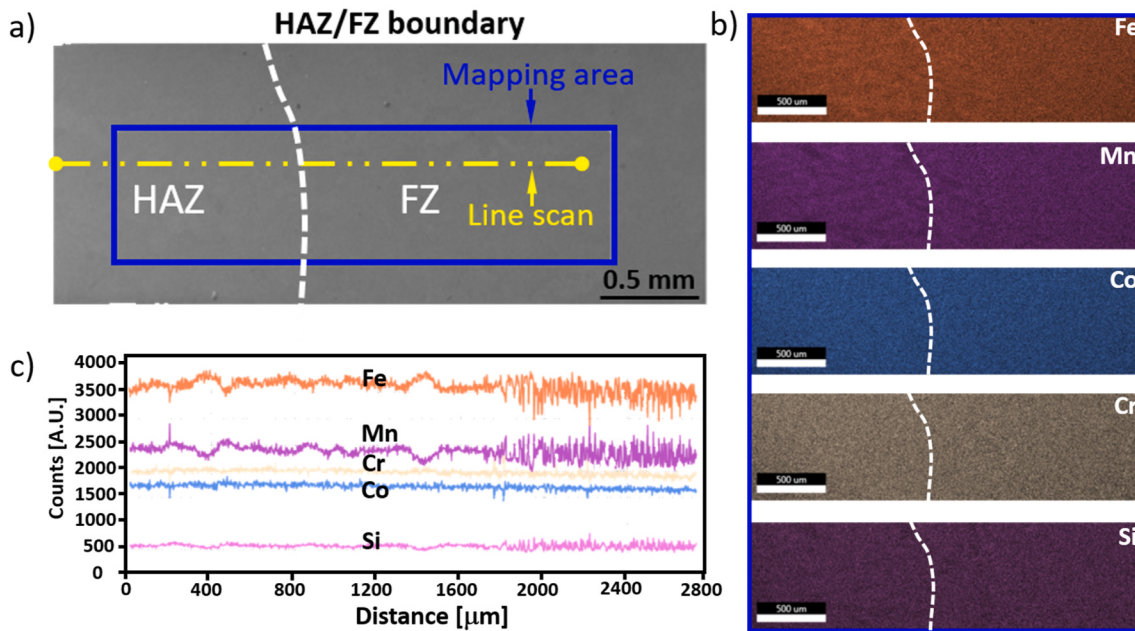


Fig. 4. a) Scanning electron microscopy (SEM) micrograph along with an energy-dispersive X-ray spectroscopy (EDS) line scan (yellow line) and area scan (blue box) near the heat affected zone/fusion zone boundary; b) EDS area mapping, with the analyzed region corresponding to the blue box of Fig. 3 a); c) EDS line scan along the yellow dashed line in Fig. 3 a). (For interpretation of the references to color in this figure legend, the reader is referred to the Web version of this article.)

grains are visible to grow in the heat affected zone, the minor growth observed can be attributed to the material's high thermal stability, which inhibits massive grain growth to occur.

Fig. 4 b) details an EDS map performed near the boundary of the heat affected zone and fusion zone for the main elements of the present HEA (Fe, Mn, Co, Cr and Si), which was used to study the homogeneity of the chemical composition of the material. The white dashed line corresponds to the boundary between the heat affected zone and fusion zone. In the heat affected zone, the chemical composition of Co, Cr, Fe, Mn and Si is well distributed in the ϵ -h.c.p. and γ -f.c.c. phases, without any segregation being observed, which is due to the fact that both the peak temperature during welding and the period at high temperatures in this region are insufficient to promote observable chemical contrast between the γ -f.c.c. and ϵ -h.c.p. phases. Within the fusion zone, elemental redistribution is a typical feature associated to the solidification of fusion-based welding process. Here, all elements are evenly distributed, suggesting that the high cooling rate during welding is beneficial for suppressing macroscopic elemental segregation.

To further present the local trends of different elements, Fig. 4 c) details an EDS line scan performed along the yellow dashed line of Fig. 4 a). From the elemental distribution curve of Fig. 4 c), there is no significant fluctuations that exist for all the elements in the heat affected zone. Taken as a whole, all elements are uniformly distributed in the heat affected zone and fusion zone. This homogeneous distribution of elements is common in metastable HEAs [6,16], unlike for Mn-containing steels [31,32], which exhibit a distinct chemical gradient across phase boundaries.

3.2. High energy synchrotron X-ray diffraction

The high photon flux and fast acquisition rate of synchrotron X-ray diffraction make it an ideal technique for advanced materials characterization. Additionally, it is capable of working in transmission mode, and the spot size is significantly smaller than when using laboratory X-ray sources. Therefore, it offers the possibility of probing processed materials at the micro to mesoscale where microstructural modifications occur, which would not be distinguished by conventional characterization approaches [33]. Here, this technique was employed to further

probe the microstructure starting from the base material and passing through the heat affected zone and fusion zone until it reached the other side of the base material. Fig. 5 a) presents the superimposition of the diffraction patterns over the entire welded joint. The extension of the base material, heat affected zone and fusion zone were determined and marked accordingly. To further compare phases that exist in the various regions of the welded joint, and to understand how the weld thermal cycle affects the microstructure, representative diffraction patterns of each location with the corresponding phase identification are shown in Fig. 5 b), c) and d), for the base material, heat affected zone and fusion zone, respectively.

Overall, X-ray diffraction peaks assigned to γ -f.c.c., ϵ -h.c.p. and σ phases exist in the base material (Fig. 5 b)), heat affected zone (Fig. 5 c)) and fusion zone (Fig. 5 c)), confirming that the gas tungsten arc welded $\text{Fe}_{42}\text{Mn}_{28}\text{Co}_{10}\text{Cr}_{15}\text{Si}_5$ joint possess the same phase structure throughout. All of the phases matched well with those previously determined using optical microscopy (refer to Fig. 2) except for σ phase, which is also well in line with the works of Gupta et al. [21] and Sittiho et al. [22], when performing friction stir welding of this metastable HEA. The presence of this dual-phase microstructure in both the heat affected and fusion zone, reveals that the thermally induced γ -f.c.c. \rightarrow ϵ -h.c.p. martensitic transformation cannot be completely kinetically inhibited by the thermal cycle experienced by these regions during the welding process [34]. For the σ phase, EDS analysis (refer to Fig. 7) will be utilized to prove the existence of this nanosized phase. Here, it is important to mention that the description of the thermally induced γ -f.c.c. \rightarrow ϵ -h.c.p. martensitic transformation will be explained further in the next section when considering the thermodynamic calculations.

Attention is now devoted to the representative X-ray diffraction patterns for three distinct regions of the joint. First, the as-cast $\text{Fe}_{42}\text{Mn}_{28}\text{Co}_{10}\text{Cr}_{15}\text{Si}_5$ base material exhibited the dual γ -f.c.c. + ϵ -h.c.p. phase structure (Fig. 5 b)), which is in line with previous reports [15]. The formation and presence of σ phase is discussed next. In HEAs of the Fe–Mn–Co–Cr system, the addition of Si and Cr increases the risk of hard and brittle σ phase formation [35]. However, the current work did not find any Cr–Si-rich particles, but rather Mn- and Si-rich particles. Frank et al. [36] previously found similarly shaped fine particles in the as-cast state of the same material, which was also detected to be rich in both Si

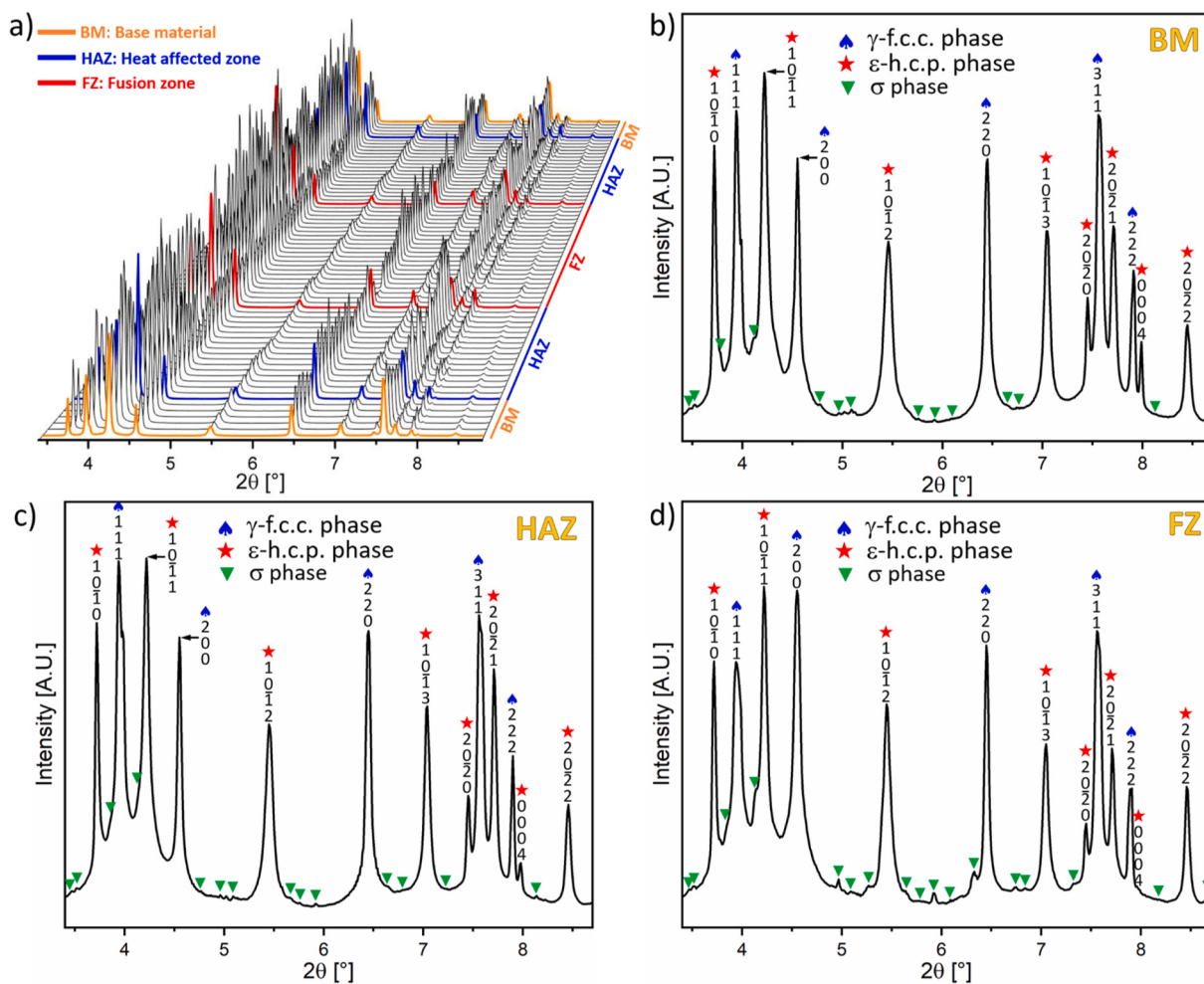


Fig. 5. a) Superimposed X-ray diffraction patterns of across the welded joint; b), c) and d) are representative diffraction patterns from the base material (BM), heat affected zone (HAZ) and fusion zone (FZ), respectively.

and Mn as determined by atom probe tomography. The authors named it as “Si phase” based on its elemental richness without determining its crystal structure. Here, the microstructure characterization of the base material, combining electron microscopy and synchrotron X-ray diffraction, allows to identify that those Si–Mn-rich precipitates are indeed σ phase with a tetragonal structure. The small intensity diffraction peaks of this phase are marked with green triangles in Fig. 5. As it will be shown in the next section, this observation is in good agreement with the thermodynamic calculations that predict the formation of a Si–Mn-rich phase upon solidification (refer to Fig. 6).

Entering the heat affected zone (Fig. 5 c)), all previously identified phases (γ -f.c.c., ε -h.c.p. and σ) were detected, suggesting that the weld thermal cycle failed to alter the phase structure in this region. Finally reaching the fusion zone, the phase identification shown in Fig. 5 d) indicates that the solidification and cooling conditions experienced by the joint region cannot prevent the same phases to be formed. It should be mentioned here that, although the weld thermal cycle is insufficient to change the existing phases in the current joint, it does alter their volume fraction, which will be further discussed below.

To quantitatively analyze of how the weld thermal cycle influenced the volume fraction of γ -f.c.c., ε -h.c.p. and σ phases across the welded joint, Rietveld refinement was performed on the synchrotron X-ray diffraction data and these results are detailed in Table 2.

As expected, the as-cast Fe₄₂Mn₂₈Co₁₀Cr₁₅Si₅ HEA showed the γ -f.c.c. phase being dominant in the dual-phase microstructure [15] with the phase distribution being $\approx 60.1\%$ of γ -f.c.c. phase, and $\approx 38.7\%$ of the

ε -h.c.p. phase. The phase fraction obtained here is consistent with the findings presented by Nene et al. [15]. These authors developed the present HEA with a metastable γ -f.c.c. dominant microstructure based on the concept of Gibbs free energy change required for the martensitic

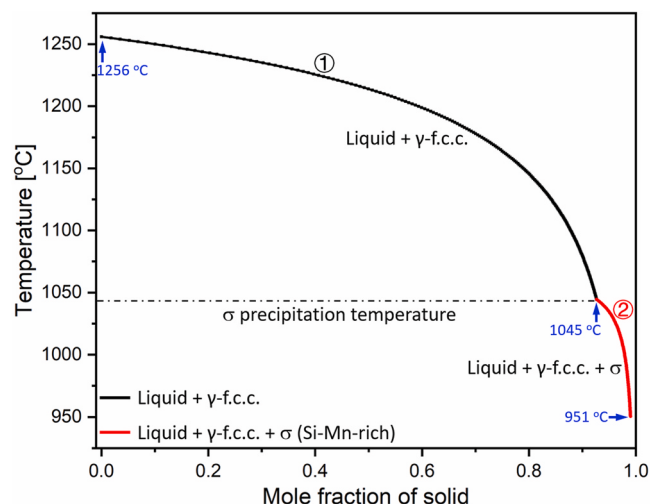


Fig. 6. Solidification path calculations using the Scheil-Gulliver model in ThermoCalc (TCHEA 5.1 database) considering the average fusion zone composition.

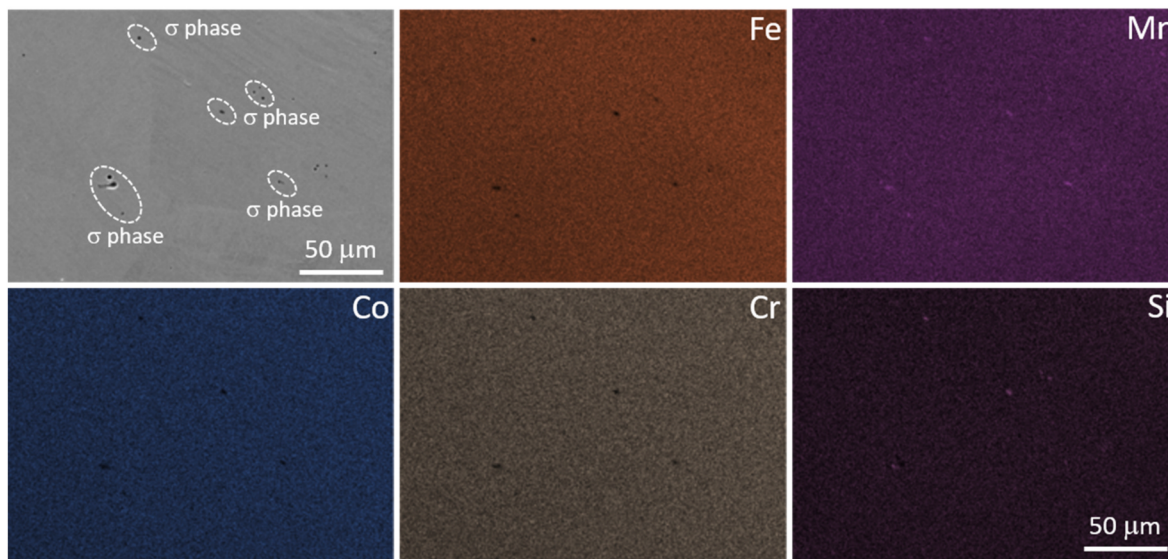


Fig. 7. SEM image and corresponding EDS mapping near particles of σ phase in the fusion zone.

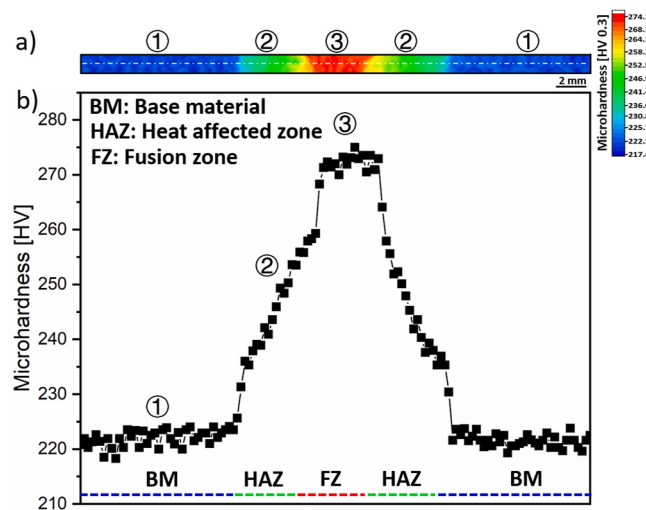


Fig. 8. a) Microhardness mapping over the welded joint; b) Microhardness distribution obtained along the mid height of the welded joint (white dashed line across the hardness map in a)).

Table 2

Volume fraction evolution of γ -f.c.c., ϵ -h.c.p. and σ phases across the welded joint (base material, heat affected zone and fusion zone) as obtained by Rietveld refinement.

Region of the welded joint	Phase volume fraction [%]		
	γ -f.c.c. phase	ϵ -h.c.p. phase	σ phase
Base material	≈60.1	≈38.7	≈1.2
Heat affected zone near the base material	≈51.3	≈47.8	≈0.9
Heat affected zone near the fusion zone	≈48.4	≈51.9	≈0.7
Fusion zone	≈73.2	≈24.4	≈2.5

transformation of γ -f.c.c. \rightarrow ϵ -h.c.p. Specifically, they modified the metastability of the γ -f.c.c. phase by increasing the Cr content and by adding Si. The Si–Mn-rich σ phase had a volume fraction of approximately ≈1.2%. The phase quantification of all existing phases in this alloy is first reported in this work. Indeed, the calculated volume

fraction of the existing phases in the base material can be considered as the phase volume fraction that should originate from an equilibrium-like solidification. Here, it should be mentioned that to avoid inhomogeneities in the cast structure near the edges of the mould walls, the sheets used for welding are taken from the central area of the casting, where the cooling conditions tend to approach an equilibrium-like condition.

The heat affected zone is the region of the welded joint where the temperature experienced allows for solid-state phase transformation to occur while remaining in the same state, i.e., solid. Interestingly, there is a significant change in the phase volume fraction of the γ -f.c.c. and ϵ -h.c.p. phases. Specifically, the γ -f.c.c. phase volume fraction decreased compared to the base material (from ≈60.1% to ≈51.3 and ≈48.4%, with the two latter values corresponding to the low and high temperature heat affected zone, respectively), and correspondingly, an increase in the volume fraction of the ϵ -h.c.p. phase was observed (from ≈38.7% to ≈47.8 and ≈51.9%). The trend in the evolution of the phase volume fraction from the base material to the heat affected zone obtained from the synchrotron data, such as the increase in the volume fraction of the ϵ -h.c.p. phase, is consistent with the trend in the phase fraction obtained from the EBSD phase maps (refer to Fig. 3 b3) and c3)). Generally, there are two ways that can trigger the γ -f.c.c. \rightarrow ϵ -h.c.p. transformation. One is via the transformation induced plasticity (TRIP) mechanism [37], the other is via a thermally-induced phase transformation [38]. In the current work, it is evident that the phase fraction of the ϵ -h.c.p. phase increases from the base material to the heat affected zone (refer to Fig. 5, Table 2, and Fig. 3 b3) and c3)). Here, the newly formed ϵ -h.c.p. laths in the heat affected zone are related to the thermally induced γ -f.c.c. \rightarrow ϵ -h.c.p. martensitic phase transformation during the welding process, and not to the TRIP effect as the eventual thermal strains that can develop during the process are not high enough to enable this mechanism. To justify that the increase in the ϵ -h.c.p. phase fraction was not related to the TRIP effect, KAM values (refer to Fig. 3 f) were used to evaluate the relationship between regions with high dislocation density and/or with a high local strain. Moreover, welding residual stresses have a correlation with the distribution of the KAM values [39], especially for welding of thin sheets, as it was demonstrated by Mitra et al. [40]. To be more specific, in Fig. 3 f, only minimum variations in the average KAM values across the welded joint exist, with 0.375°, 0.451° and 0.625° for the base material, heat affected zone and fusion zone, respectively, which allows to infer the minimal residual strain/stress within the welded joint induced by the weld thermal cycle. Thus, the low residual stress/strain deduced from the KAM analysis, justifies the reasonableness of the

hypothesis that the ϵ -h.c.p. transformation from the parent γ -f.c.c. occurred by a thermal-induced process, rather than by a deformation-assisted one. In conclusion, the γ -f.c.c. to ϵ -h.c.p. martensitic phase transformation that occurs in the heat affected zone is attributed to an allotropic transformation during cooling [41], i.e., the migration and rearrangement of atoms during the cooling process.

In other words, variations in both the local cooling rate and on the grain size affect the phase stability in metastable HEAs, where the higher cooling rates enhances the stability of the high temperature γ -f.c.c. phase while the large grains aid in stabilizing the ϵ -h.c.p. phase [42]. The reason for the increased volume fraction of the ϵ -h.c.p. phase in the heat affected zone is, thus, due to the thermal cycle experienced by the material. The maximum temperature at which the ϵ -h.c.p. phase is stable is 425 °C [15]. Hence, any region of the material that experiences temperatures above this will transform to γ -f.c.c. However, within the heat affected zone, the distance to the heat source will influence both the peak temperature, as well as the associated cooling rate, leading to a gradient in the fraction of γ -f.c.c. and ϵ -h.c.p. across this region which impacts the local mechanical properties, as it will be shown latter. For the relationship between the cooling rate and the thermal induced phase transformation from γ -f.c.c. to ϵ -h.c.p., the closer to the boundary of the heat affected zone/fusion zone the faster the cooling rate. With faster cooling rate the easier it is for the formation of the low-temperature ϵ -h.c.p. phase to be inhibited [30,38], which leads to more γ -f.c.c. phase being stabilized. Therefore, purely considering the effect of the cooling rate on the γ -f.c.c. to ϵ -h.c.p. phase transformation, the phase volume fraction of the high temperature stable γ -f.c.c. phase will increase and ϵ -h.c.p. phase should decrease, since the cooling rate increases from the base material to the fusion zone [44]. However, it was observed that the volume fraction of the γ -f.c.c. phase is decreasing, with a concomitant increase in the ϵ -h.c.p. phase content (refer to Table 2), which is contrary to the results expected from the current analysis considering the effect of the cooling rate detailed above. However, as detailed before, for metastable HEAs, the phase evolution depends on a competition between both the cooling rate and the grain size, and not solely on the variation of one or the other [21]. Hence, this requires a continuation of the analysis in terms of the variation of the grain size and the phase transformation.

Contrary to the effect of increasing the cooling rate on the phase transformation, an increase in grain size promotes the γ -f.c.c. to ϵ -h.c.p. phase transformation [43]. In other words, an increase in grain size reduces the phase volume fraction of γ -f.c.c., while increasing the volume fraction of the ϵ -h.c.p. In the current work, from the base material into the heat affected zone, the grain structure is coarsened (refer to Fig. 3 e)) due to the increase in peak temperature and permanence time for grain growth to occur. This will promote the ϵ -h.c.p. stability, favouring the γ -f.c.c. to ϵ -h.c.p. martensitic phase transformation upon cooling after welding. Thus, two concurring effects, namely grain size and cooling rate, will compete towards the stability of the γ -f.c.c. or the ϵ -h.c.p. phases. However, based on the above analysis, it can be deduced that, in the present work, the competition between cooling rate and grain size growth on thermal induced phase transformation is more influenced by the changes in grain size. In other words, the increase in grain size dominates the phase fraction evolution from the base material to the heat affected zone, promoting a stabilization of the ϵ -h.c.p. instead.

In what matters σ phase, there is a partial dissolution, as its volume fraction is reduced from 1.2% in the base material to 0.9% in the heat affected zone and then to 0.7% when approaching the fusion zone boundary. It is worth mentioning here that in the current work, the σ phase can be formed in two ways, one way is being formed directly from the rapid solidification of the melt pool at the end of the solidification (refer to Fig. 6), while another way is forming upon precipitation upon cooling until ≈ 400 °C. As mentioned before, the base material sheets used for welding in this work were taken from the central area of a large casting, where cooling is slow so that there is sufficient time for σ phase to form during the cooling process. Thus, it can be inferred that the

volume fraction of the 1.2% of σ phase in the base material is predominantly formed in the slow cooling process during casting. Now, one must consider the thermally affected regions and the thermodynamic calculations that predicted a melting point for σ phase to be close to 1045 °C. Thus, in the heat affected zone that experience temperatures below 1045 °C, there will be a preservation of this phase. However, still in the heat affected zone, but in regions where the peak temperature surpassed 1045 °C, the phase fraction of σ starts to decrease which can be attributed to partial dissolution. It should be mentioned that the non-equilibrium heating/cooling conditions experienced during welding can also promote a shift in the temperatures at which certain solid state transformations occur. So, the thermodynamically predicted melting temperature of σ phase is only used as a qualitative reference to unveil the partial dissolution or not of this phase due to the weld thermal cycle in the heat affected zone. The present analysis predicts a trend in the volume fraction variation of σ phase based on the pathway of σ phase formation and the effect of weld thermal cycle on this phase, which is consistent with the trend in the volume fraction of the σ phase obtained from the synchrotron data.

It is well known that the fusion zone is the region of a welded joint that undergoes melting and fast, non-equilibrium solidification. Here, a significant change in the phase volume fraction of both γ -f.c.c. and ϵ -h.c.p. phases is noted, with the volume fraction of the γ -f.c.c. phase increasing from 60.1% (in base material) to 73.2%, while the ϵ -h.c.p. phase retained only 24.4%. This is mainly ascribed to the higher cooling rate in the fusion zone compared to that experienced during casting of the present base material [44]. Specifically, for metastable HEAs with low stacking fault energy, as the present material, γ -f.c.c. and ϵ -h.c.p. phases are the stable phases at high and low temperatures, respectively [45]. The volume fraction of the ϵ -h.c.p. phase is strongly dependent on the cooling rate [38]. Thus, in the fusion zone, the thermally induced γ -f.c.c. to ϵ -h.c.p. martensitic transformation could be kinetically inhibited due to the faster cooling rate observed during welding than during casting, enabling to retain more metastable γ -f.c.c. phase. Thus, the variation in the volume fraction of γ -f.c.c. and ϵ -h.c.p. phases in the fusion zone compared to the base material suggests that the cooling rate is the primary reason affecting the extent of the γ -f.c.c. to ϵ -h.c.p. martensitic phase transformation in this metastable HEA. Similarly, although the peak temperature in the heat affected zone, can enable to experience solid state phase transformations, it is still lower than the peak temperature of the fusion zone. Based on the relationship between peak temperature and cooling rate [46], it can be stated that the cooling rate in the fusion zone is higher than in the heat affected zone even at the γ -f.c.c. to ϵ -h.c.p. phase transformation temperature point (425 °C). Further observing the phase volume fraction distribution, the volume fraction of the γ -f.c.c. phase increases and ϵ -h.c.p. phase decreases, suggesting again that the fast cooling rate in the fusion zone can kinetically inhibit the thermally induced γ -f.c.c. to ϵ -h.c.p. phase transformation, even though there is evidence of grain growth in this region. This phenomenon of inhibiting the martensitic phase transformation in the fusion zone due to rapid non-equilibrium solidification was also reported in the study of Zhu et al. [34]. It is worth mentioning here that, in Fig. 5 d), the X-ray diffraction peaks corresponding to the ϵ -h.c.p. phase possess high intensity, similar to that of the γ -f.c.c. phase, which is due to the strong texture effect in the ϵ -h.c.p. phase promoted by the rapid solidification in the fusion zone, rendering a highly oriented grain structure. For the σ phase, it can be observed that an increased volume fraction exists in the fusion zone compared to the remaining regions of the joint ($\approx 2.5\%$ for the fusion zone, $\approx 0.9\%$ for the heat affected zone and $\approx 1.2\%$ for the base material), this can be further evidenced by the higher peak intensity of σ phase as shown in X-ray diffractogram of Fig. 5 d)). This phenomenon occurs as a result of the addition of Si that leads to the Si-Mn-rich σ phase being generated directly from the rapid solidification of the melt pool at the end of the solidification (more details on this will be provided when discussing the thermodynamic data of Fig. 6), which is consistent with the findings

reported by Nene et al. whom used thermodynamic calculations to investigate the effect of Si on the σ phase formation [35]. In addition, a small amount of σ phase can also precipitate. Although they can be formed at different times (from solidification and upon cooling in the solid state) they share the same tetragonal crystal structure and the same chemical enrichment in both Si and Mn. Based on the above analysis, the amount of σ in the fusion zone differs from that in the base material and the heat affected zone due to the fact that the main source of the σ phase from the fusion zone is solidification precipitation, while the predominant source of the σ phase from the base material and the heat affected zone is cooling precipitation. However, in either case, σ phase is enriched in both Si and Mn. It should also be mentioned that the present work does not quantify the volume fraction of σ phase arising from different sources, as is not within the scope of this study.

3.3. Thermodynamic calculations

In order to gain a better understanding of the solidification process that occurs in the fusion zone, the Scheil-Gulliver model was used to implement and predict the solidification pathway and phases formation in the fusion zone by considering the non-equilibrium solidification conditions. As determined by EDS measurements, the average fusion zone composition (35% Fe, 23% Mn, 17% Co, 19% Cr and 6% Si, at. %) was used for these thermodynamic calculations. Besides, a nominal composition of the material was also taken into account (42% Fe, 28% Mn, 10% Co, 15% Cr and 5% Si, at. %) to perform the same calculations.

Although not shown here, when comparing the non-equilibrium solidification diagrams obtained with the two different compositions it was found that the solidification pathway, as well as the phases formed, are practically the same. As a matter of fact, the only subtle differences between the two (average vs nominal compositions) are the temperatures of the solidus and liquidus as well as the temperature at which the σ phase begins to form. Thus, here, only the non-equilibrium solidification pathway obtained considering the average measured composition of the fusion zone is analyzed, as shown in Fig. 6.

As can be clearly seen in Fig. 6, the solidification path takes place in two steps as follows: Liquid \rightarrow Liquid + γ -f.c.c., then followed by γ -f.c.c. and σ phases being formed from the remaining liquid. When using the average fusion zone composition, the solidus and liquidus temperatures were determined to be 951 and 1256 °C, respectively, whereas the range for σ formation occurred between 1045 and 951 °C. For reference, the liquidus, solidus and σ formation temperatures are 1223, 915, 932 and 916 °C when using the nominal composition of the material. It is worth noting that there is no trace of the ϵ -h.c.p. phase during the solidification process presented in Fig. 6. In fact, the ϵ -h.c.p. phase previously detected in the fusion zone by synchrotron X-ray diffraction data (refer to Fig. 5 d)) and optical microscopy (refer to Fig. 2), did not form directly from the liquid, but rather occurred during a solid-state phase transformation upon further cooling after solidification was finished. This again proved the previous assumption that the variation of the γ -f.c.c. and ϵ -h.c.p. phases volume fraction in the heat affected zone and fusion zone are the result of a thermally induced γ -f.c.c. \rightarrow ϵ -h.c.p. martensitic phase transformation.

According to these thermodynamic calculations, the σ phase that formed during non-equilibrium solidification was enriched in both Si and Mn. Furthermore, EDS data details that these small particles observed in the fusion zone are also enriched in both Si and Mn (see Fig. 7), which further validates these thermodynamic calculations. This will be discussed in detail next.

The EDS mapping of the constituent elements (Fe, Mn, Co, Cr and Si) was conducted to further investigate the composition distribution of the fine black particles that can be observed in the fusion zone, which are shown in the SEM images of Fig. 7 with white ellipses. These EDS data confirms that these black particles are enriched in both Mn and Si, suggesting that these two elements had the most significant tendency to cluster [47]. Interestingly, in the present work, Mn and Si were also the

elements with the most significant discrepancies in electronegativity [48] in the Fe–Mn–Co–Cr–Si system. Nene et al. [15] previously used atom probe tomography reconstruction to identify short-range clusters by nearest neighbor analysis of the particles that appeared in the same Fe–Mn–Co–Cr–Si metastable HEA. The observed elemental clustering is consistent with the current work observations, i.e., the particles being Si–Mn-rich. In conclusion, the Si–Mn-rich particles detected by EDS matched with the thermodynamically predicted σ phase enrichment of these two elements (refer to Fig. 6), thus validating the accuracy of the thermodynamic predictions.

3.4. Mechanical behavior

Generally, there two main factors that will affect the hardness of a material, one is the variation in grain size and the other are changes in the phase volume fraction. A detailed analysis as to which mechanism predominantly dominates across the joint is detailed next.

As shown in Fig. 8, microhardness measurements were performed across the welded joint to further evaluate how the weld thermal cycle and local material microstructure effected the local material strength. The color change in the hardness mapping presented in Fig. 8 a) identified three typical regions of the welded joint: the blue, green and red colors represent the base material, heat affected zone and fusion zone, respectively, and these regions have been marked by a different number each. Besides, a representative trend of the hardness variation along the joint, obtained at mid height, is detailed in Fig. 8 b).

From Fig. 8 b), a significant difference in hardness was found among the base material (≈ 221 HV0.3), heat affected zone (ranging from ≈ 225 to ≈ 262 HV0.3) and fusion zone (≈ 275 HV0.3). As can be seen, the hardness in the region of the base material is the lowest of all, whereas the heat affected zone has an increasing trend in hardness value when compared to the base material. The increase in hardness in the heat affected zone when moving towards the fusion boundary is mainly due to a higher phase volume fraction of the hard ϵ -h.c.p. phase (increased from 38.7 to 47.8%), which increases similarly along the heat affected zone (refer to Table 2). Previously, Hou et al. [51] and Shaysultanov et al. [52] reported that the hardness of the ϵ -h.c.p. phase is approximately three times higher than that of the γ -f.c.c. phase in such

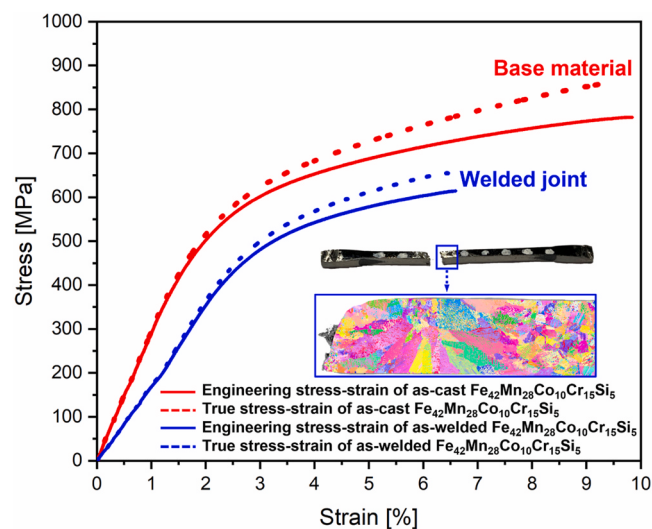


Fig. 9. Engineering and true tensile stress-strain curves of base material (red solid line and dashed red line, respectively) and engineering and true tensile stress-strain curves of as-welded as-cast $\text{Fe}_{42}\text{Mn}_{28}\text{Co}_{10}\text{Cr}_{15}\text{Si}_5$ metastable HEA (blue solid line and blue dashed line, respectively). The blue box corresponds to the EBSD data, which highlighted the inserts of the fracture site. (For interpretation of the references to color in this figure legend, the reader is referred to the Web version of this article.)

Table 3

Summary of tensile properties of BM, gas tungsten arc welded Fe₄₂Mn₂₈-Co₁₀Cr₁₅Si₅ joints.

	Yield strength [MPa]	Ultimate tensile strength [MPa]	Fracture strain [%]
Base material	≈440	≈790	≈9.8
Welded joints	≈400	≈615	≈6.6

metastable HEAs. From the base material region, entering into the heat affected zone, the average grain size of the matrix γ -f.c.c. increases from 47.5 μm (base material) to 54.2 μm (heat affected zone), which should result in a minor hardness decrease following the Hall-Petch relationship. However, the fact is that the hardness increases from 221 HV0.3 in the base material region to the heat affected zone (225 HV). Although there is an increase in the grain size when approaching the fusion boundary, the observed increase in hardness is due to the higher ϵ -h.c.p. phase fraction, which promotes an obvious strengthening along the heat affected zone. Based on the above analysis, it can be deduced that the change in phase fraction is the predominant factor for the increased hardness within the heat affected zone, despite the existence of a coarse grain structure.

One interesting feature is the hardness distribution in the fusion zone. If purely looking at the volume fractions of γ -f.c.c. (73.2%) and ϵ -h.c.p. (24.4%) phases, it would be expected that a smaller hardness would exist at this region, owing to the domination of a soft γ -f.c.c. microstructure. In contrast, the fusion zone showed a maximum value of hardness over the whole joint, which was mainly due to the very refined subgrain structure of both the γ -f.c.c. and ϵ -h.c.p. product phase ($\approx 2 \mu\text{m}$) induced by the relatively rapid solidification of the fusion zone (refer to Fig. 2 b4), and the consequent introduction of fine grain strengthening, which compensates for the loss of the hardness by the dominance of the soft γ -f.c.c. phase. Thus, although the volume fraction of ϵ -h.c.p. phase is lower in the fusion zone, the substantial grain refinement is enough to significantly increase the material hardness at this location.

To assess the mechanical performance of the welded joints, and compare them with the base material, uniaxial tensile testing until

failure was carried out on both gas tungsten arc welded Fe₄₂Mn₂₈-Co₁₀Cr₁₅Si₅ joints, as well as the as-cast Fe₄₂Mn₂₈-Co₁₀Cr₁₅Si₅ base material. Fig. 9 provides the engineering and true stress-strain curves for the as-welded joints (blue solid and dashed curve) and as-cast base material (red solid and dashed color). Detailed information on the mechanical properties of the materials discussed above can be found in Table 3.

Overall, both the strength and ductility of the welds are decreased compared to the base material. More specifically, the engineering yield strength, ultimate tensile strength and maximum elongation of the base material (subtracting the elastic regime) are ≈ 440 MPa, ≈ 790 MPa and ≈ 8.6% respectively, while for the welded joints these values are ≈ 400 MPa, ≈ 615 MPa and ≈ 4.5%. It is important to note that although the joints exhibit an inferior performance than the original base material for both ultimate strength and ductility, they still exhibit interesting mechanical properties, with the potential to be used in structural applications. Based on the macroscopic characteristics of the fracture in the joints, it can be concluded that failure took place in the fusion zone. To further verify the fracture site, EBSD analysis was performed on the tensile specimen after fracture, detailed in the insert of Fig. 9. Based on the strong crystal orientation shown in the IPF maps, it can be also confirmed that the fracture occurred in the fusion zone, though almost approaching the fusion boundary. The larger amount (relative to the base material and heat affected zone) of hard σ phase that was determined to exist in this region can justify the fracture location. Moreover, the nearly twice volume fraction of σ phase that exists in the fusion zone, which can act as stress concentrators, trigger crack initiation and subsequent development, it can also contribute to the premature failure of the joint as well as its location.

Theoretically, TWIP and TRIP effects occur during the deformation of metastable HEAs, which can improve the strength and ductility of the material [6,17]. However, based on the final mechanical behavior of the welded joint in the current work (refer to Fig. 9), it can be speculated that the large amount of nanosized σ phase distributed in the fusion zone triggers localized stress concentrations and cracking sources, causing the joints to fracture prematurely and not allowing the TWIP and TRIP effects to fully exploit their advantages in improving the mechanical properties of the material. Hence, future work will be primarily focused

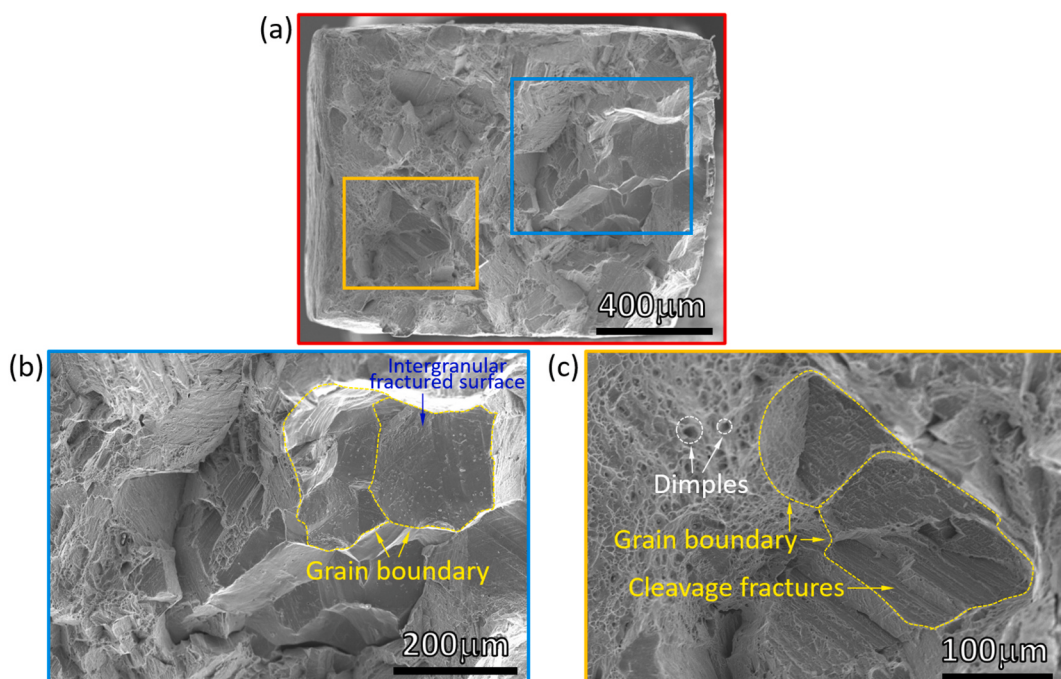


Fig. 10. a) a overview of fracture surface of welded joint; b) and c) close-up detailing the ductile and brittle characteristics.

on how to improve the mechanical properties of the current welded joints by using post-weld heat treatments.

To further explore the fracture mode as well as to determine the fracture origin, the tensile fracture morphology of the as-welded joints of Fe₄₂Mn₂₈Co₁₀Cr₁₅Si₅ metastable HEA were observed by SEM, as shown in Fig. 10. Fig. 10 a) details the overview of the fracture surface with Fig. 10 b) and 10 c) detailing zoomed in images of specific features observed. Interestingly, an intergranular fractured surface was observed, as shown in Fig. 10 b). This implies that slip location is helpful in facilitating the development of damage along the grain boundaries [49]. As marked in Fig. 10 c), evidence of cleavage fractures and dimples reveal a mixed brittle and ductile fracture morphologies.

Normally, localized plasticity in metastable HEAs can promote intergranular cracking mechanisms [50]. Considering that the hard nanosized σ phase was mainly distributed near the phase boundaries (refer to Fig. 2), it can be deduced that the stress concentration induced by the σ phase activates localized plastic deformation at the grain boundaries, which aids in crack initiation occurring near the boundaries, and eventually fracture occurs along the grain boundaries. In addition, the brittle ϵ -h.c.p. phase induced by the TRIP effect during tensile loading, tends to nucleate and grow near the grain boundaries, further reducing the ductility at the grain boundaries and serves as an auxiliary mechanism for localized plastic deformation. Thus, the analysis of the fracture mechanism further validates the previous hypothesis that the higher volume fraction of the hard nanosized σ phase in the fusion zone is the main reason for inducing premature failure in this region of the welded joint.

4. Conclusions

A combination of advanced materials characterization and thermodynamic calculations was used to investigate the how gas tungsten arc welding affects the microstructure and mechanical properties of an as-cast Fe₄₂Mn₂₈Co₁₀Cr₁₅Si₅ metastable high entropy alloy. In conclusion, the following main points can be made.

- Overall, there were no welding defects detected in the joints, which exhibited a good weldability.
- The γ -f.c.c. to ϵ -h.c.p. phase transformation in the heat affected zone and fusion zone does not occur due to the TRIP effect triggered by the weld thermal strains, but rather due to a thermally-induced martensitic phase transformation during the cooling process.
- Competition between grain size and locally varying cooling rates were seen to influence the phase stability across the heat affected zone.
- Microstructure characterization, combining electron microscopy and synchrotron X-ray diffraction determined that Si-Mn-rich precipitates are σ phase with a tetragonal structure, which in good agreement with the thermodynamic calculations used to predict the solidification pathway.
- The cooling rate is the primary reason affecting the extent of γ -f.c.c. to ϵ -h.c.p. martensitic phase transformation in the fusion zone.
- Although the phase volume fraction of hard ϵ -h.c.p. significantly reduced in the fusion zone, the refine grain size of this phase promoted a significant strengthening effect at this location.
- The joints have a lower strength and ductility compared to the original base material, but can still be considered for structural applications owing to their good mechanical performance.

The raw/processed data required to reproduce these findings cannot be shared at this time as the data also forms part of an ongoing study.

CRediT authorship contribution statement

Jiajia Shen: Investigation, Formal analysis, Data curation, Methodology, Writing – original draft. **Priyanka Agrawal:** Investigation,

Formal analysis, Writing – review & editing. **Tiago A. Rodrigues:** Investigation. **J.G. Lopes:** Investigation. **N. Schell:** Investigation. **Jingjing He:** Investigation. **Zhi Zeng:** Investigation. **Rajiv S. Mishra:** Validation, Writing – review & editing. **J.P. Oliveira:** Formal analysis, Supervision, Resources, Validation, Conceptualization, Methodology, Writing – review & editing.

Declaration of competing interest

The authors declare that they have no known competing financial interests or personal relationships that could have appeared to influence the work reported in this paper.

Data availability

Data will be made available on request.

Acknowledgments

JS, JGL and JPO acknowledge Fundação para a Ciência e a Tecnologia (FCT - MCTES) for its financial support via the project UID/00667/2020 (UNIDEMI). JPO acknowledges funding by national funds from FCT - Fundação para a Ciência e a Tecnologia, I.P., in the scope of the projects LA/P/0037/2020, UIDP/50025/2020 and UIDB/50025/2020 of the Associate Laboratory Institute of Nanostructures, Nanomodelling and Nanofabrication – i3N. JS acknowledges the China Scholarship Council for funding the Ph.D. grant (CSC NO. 201808320394). JGL acknowledges FCT – MCTES for funding the Ph.D. grant 2020.07350.BD. TAR acknowledges FCT – MCTES for funding the Ph.D. grant SFRH/BD/144202/2019. The authors acknowledge DESY (Hamburg, Germany), a member of the Helmholtz Association HGF, for the provision of experimental facilities. Beamtime was allocated for proposal I-20220492 EC. The research leading to this result has been supported by the project CALIPSOplus under the Grant Agreement 730872 from the EU Framework Programme for Research and Innovation HORIZON 2020.

References

- [1] Y.F. Ye, Q. Wang, J. Lu, C.T. Liu, Y. Yang, High-entropy alloy: challenges and prospects, Mater. Today 19 (2016) 349–362, <https://doi.org/10.1016/j.matto.2015.11.026>.
- [2] Z. Wang, W. Qiu, Y. Yang, C.T. Liu, Atomic-size and lattice-distortion effects in newly developed high-entropy alloys with multiple principal elements, Intermetallics 64 (2015) 63–69, <https://doi.org/10.1016/j.intermet.2015.04.014>.
- [3] J.W. Yeh, Y.L. Chen, S.J. Lin, S.K. Chen, High-entropy alloys – a new era of exploitation, Mater. Sci. Forum 560 (2007) 1–9, <https://doi.org/10.4028/www.scientific.net/MSF.560.1>.
- [4] E.J. Pickering, N.G. Jones, High-entropy alloys: a critical assessment of their founding principles and future prospects, Int. Mater. Rev. 61 (2016) 183–202, <https://doi.org/10.1080/09506608.2016.1180020>.
- [5] J. Dąbrowska, M. Zajusz, W. Kucza, G. Cieślak, K. Berent, T. Czeppe, T. Kulik, M. Danielewski, Demystifying the sluggish diffusion effect in high entropy alloys, J. Alloys Compd. 783 (2019) 193–207, <https://doi.org/10.1016/j.jallcom.2018.12.300>.
- [6] Z. Li, K.G. Pradeep, Y. Deng, D. Raabe, C.C. Tasan, Metastable high-entropy dual-phase alloys overcome the strength–ductility trade-off, Nature 534 (2016) 227–230, <https://doi.org/10.1038/nature17981>.
- [7] P. Sathiayamoorthi, J. Basu, S. Kashyap, K.G. Pradeep, R.S. Kottada, Thermal stability and grain boundary strengthening in ultrafine-grained CoCrFeNi high entropy alloy composite, Mater. Des. 134 (2017) 426–433, <https://doi.org/10.1016/j.matdes.2017.08.053>.
- [8] J. Wang, S. Wu, S. Fu, S. Liu, M. Yan, Q. Lai, S. Lan, H. Hahn, T. Feng, Ultrahigh hardness with exceptional thermal stability of a nanocrystalline CoCrFeNiMn high-entropy alloy prepared by inert gas condensation, Scripta Mater. 187 (2020) 335–339, <https://doi.org/10.1016/j.scriptamat.2020.06.042>.
- [9] J.R. Scully, S.B. Inman, A.Y. Gerard, C.D. Taylor, W. Windl, D.K. Schreiber, P. Lu, J. E. Saal, G.S. Frankel, Controlling the corrosion resistance of multi-principal element alloys, Scripta Mater. 188 (2020) 96–101, <https://doi.org/10.1016/j.scriptamat.2020.06.065>.
- [10] H. Luo, S.S. Sohn, W. Lu, L. Li, X. Li, C.K. Soundararajan, W. Krieger, Z. Li, D. Raabe, A strong and ductile medium-entropy alloy resists hydrogen embrittlement and corrosion, Nat. Commun. 11 (2020) 3081, <https://doi.org/10.1038/s41467-020-16791-8>.

- [11] B. Gludovatz, A. Hohenwarter, D. Catoor, E.H. Chang, E.P. George, R.O. Ritchie, A fracture-resistant high-entropy alloy for cryogenic applications, *Science* 345 (2014) 1153–1158, <https://doi.org/10.1126/science.1254581>.
- [12] S.J. Sun, Y.Z. Tian, H.R. Lin, H.J. Yang, X.G. Dong, Y.H. Wang, Z.F. Zhang, Achieving high ductility in the 1.7 GPa grade CoCrFeMnNi high-entropy alloy at 77 K, *Mater. Sci. Eng., A* 740–741 (2019) 336–341, <https://doi.org/10.1016/j.msea.2018.10.094>.
- [13] F. Otto, A. Dlouhý, C. Somsen, H. Bei, G. Eggeler, E.P. George, The influences of temperature and microstructure on the tensile properties of a CoCrFeMnNi high-entropy alloy, *Acta Mater.* 61 (2013) 5743–5755, <https://doi.org/10.1016/j.actamat.2013.06.018>.
- [14] Z. Li, D. Raabe, Strong and ductile non-equiautomic high-entropy alloys: design, processing, microstructure, and mechanical properties, *J. Occup. Med.* 69 (2017) 2099–2106, <https://doi.org/10.1007/s11837-017-2540-2>.
- [15] S.S. Nene, M. Frank, K. Liu, R.S. Mishra, B.A. McWilliams, K.C. Cho, Extremely high strength and work hardening ability in a metastable high entropy alloy, *Sci. Rep.* 8 (2018) 9920, <https://doi.org/10.1038/s41598-018-28383-0>.
- [16] Z. Li, C.C. Tasan, H. Springer, B. Gault, D. Raabe, Interstitial atoms enable joint twinning and transformation induced plasticity in strong and ductile high-entropy alloys, *Sci. Rep.* 7 (2017), 40704, <https://doi.org/10.1038/srep40704>.
- [17] Z. Li, C.C. Tasan, K.G. Pradeep, D. Raabe, A TRIP-assisted dual-phase high-entropy alloy: grain size and phase fraction effects on deformation behavior, *Acta Mater.* 131 (2017) 323–335, <https://doi.org/10.1016/j.actamat.2017.03.069>.
- [18] R.S. Haridas, P. Agrawal, S. Yadav, P. Agrawal, A. Gumaste, R.S. Mishra, Work hardening in metastable high entropy alloys: a modified five-parameter model, *J. Mater. Res. Technol.* 18 (2022) 3358–3372, <https://doi.org/10.1016/j.jmrt.2022.04.016>.
- [19] P. Agrawal, S. Gupta, S. Shukla, S.S. Nene, S. Thapliyal, M.P. Toll, R.S. Mishra, Role of Cu addition in enhancing strength-ductility synergy in transforming high entropy alloy, *Mater. Des.* 215 (2022), 110487, <https://doi.org/10.1016/j.matdes.2022.110487>.
- [20] S.S. Nene, S. Gupta, C. Morphew, R.S. Mishra, Friction stir butt welding of a high strength Al-7050 alloy with a metastable transformative high entropy alloy, *Materialia* 11 (2020), 100740, <https://doi.org/10.1016/j.mtla.2020.100740>.
- [21] S. Gupta, P. Agrawal, S.S. Nene, R.S. Mishra, Friction stir welding of γ -fcc dominated metastable high entropy alloy: microstructural evolution and strength, *Scripta Mater.* 204 (2021), 114161, <https://doi.org/10.1016/j.scriptamat.2021.114161>.
- [22] A. Sittihi, M. Bhattacharyya, J. Graves, S.S. Nene, R.S. Mishra, I. Charit, Friction stir processing of a high entropy alloy Fe42Co10Cr15Mn28Si5 with transformative characteristics: microstructure and mechanical properties, *Mater. Today Commun.* 28 (2021), 102635, <https://doi.org/10.1016/j.mtcomm.2021.102635>.
- [23] J.-O. Andersson, T. Helander, L. Höglund, P. Shi, B. Sundman, Thermo-Calc & DICTRA, computational tools for materials science, *Calphad* 26 (2002) 273–312, [https://doi.org/10.1016/S0364-5916\(02\)00037-8](https://doi.org/10.1016/S0364-5916(02)00037-8).
- [24] P. Schaffnit, C. Stallybrass, J. Konrad, F. Stein, M. Weinberg, A Scheil-Gulliver model dedicated to the solidification of steel, *Calphad* 48 (2015) 184–188, <https://doi.org/10.1016/j.calphad.2015.01.002>.
- [25] A. Sittihi, M. Bhattacharyya, J. Graves, S.S. Nene, R.S. Mishra, I. Charit, Friction stir processing of a high entropy alloy Fe42Co10Cr15Mn28Si5 with transformative characteristics: microstructure and mechanical properties, *Mater. Today Commun.* 28 (2021), 102635, <https://doi.org/10.1016/j.mtcomm.2021.102635>.
- [26] J. Ahmed, M. Daly, Yield strength insensitivity in a dual-phase high entropy alloy after prolonged high temperature annealing, *Mater. Sci. Eng.* 820 (2021), 141586, <https://doi.org/10.1016/j.msea.2021.141586>.
- [27] S.A. David, S.S. Babu, J.M. Vitek, Welding: solidification and microstructure, *J. Occup. Med.* 55 (2003) 14–20, <https://doi.org/10.1007/s11837-003-0134-7>.
- [28] W. Kurz, C. Bezençon, M. Gäumann, Columnar to equiaxed transition in solidification processing, *Sci. Technol. Adv. Mater.* 2 (2001) 185–191, [https://doi.org/10.1016/S1468-6996\(01\)00047-X](https://doi.org/10.1016/S1468-6996(01)00047-X).
- [29] X. Liu, R. Banerjee, L. Vitos, Y. Wang, Metastable high entropy alloys, *Appl. Phys. Lett.* 120 (2022), 120401, <https://doi.org/10.1063/5.0091351>.
- [30] W. Zhang, J. Shen, J.P. Oliveira, B.J. Kooi, Y. Pei, Crystallographic orientation-dependent deformation characteristics of additive manufactured interstitial-strengthened high entropy alloys, *Scripta Mater.* 222 (2023), 115049, <https://doi.org/10.1016/j.scriptamat.2022.115049>.
- [31] O. Dmitrieva, D. Ponge, G. Inden, J. Millán, P. Choi, J. Sietsma, D. Raabe, Chemical gradients across phase boundaries between martensite and austenite in steel studied by atom probe tomography and simulation, *Acta Mater.* 59 (2011) 364–374, <https://doi.org/10.1016/j.actamat.2010.09.042>.
- [32] D. Raabe, S. Sandlöbes, J. Millán, D. Ponge, H. Assadi, M. Herbig, P.-P. Choi, Segregation engineering enables nanoscale martensite to austenite phase transformation at grain boundaries: a pathway to ductile martensite, *Acta Mater.* 61 (2013) 6132–6152, <https://doi.org/10.1016/j.actamat.2013.06.055>.
- [33] Q. Guo, M. Qu, C.A. Chuang, L. Xiong, A. Nabaa, Z.A. Young, Y. Ren, P. Kenesei, F. Zhang, L. Chen, Phase transformation dynamics guided alloy development for additive manufacturing, *Addit. Manuf.* 59 (2022), 103068, <https://doi.org/10.1016/j.addma.2022.103068>.
- [34] Z.G. Zhu, X.H. An, W.J. Lu, Z.M. Li, F.L. Ng, X.Z. Liao, U. Ramamurty, S.M.L. Nai, J. Wei, Selective laser melting enabling the hierarchically heterogeneous microstructure and excellent mechanical properties in an interstitial solute strengthened high entropy alloy, *Materials Research Letters* 7 (2019) 453–459, <https://doi.org/10.1080/21663831.2019.1650131>.
- [35] S.S. Nene, M. Frank, P. Agrawal, S. Sinha, K. Liu, S. Shukla, R.S. Mishra, B. A. McWilliams, K.C. Cho, Microstructurally flexible high entropy alloys: linkages between alloy design and deformation behavior, *Mater. Des.* 194 (2020), 108968, <https://doi.org/10.1016/j.matdes.2020.108968>.
- [36] M. Frank, S.S. Nene, Y. Chen, B. Gwalani, E.J. Kautz, A. Devaraj, K. An, R. S. Mishra, Correlating work hardening with co-activation of stacking fault strengthening and transformation in a high entropy alloy using in-situ neutron diffraction, *Sci. Rep.* 10 (2020), 22263, <https://doi.org/10.1038/s41598-020-7949-8>.
- [37] R.S. Mishra, S.S. Nene, Some unique aspects of mechanical behavior of metastable transformative high entropy alloys, *Metall. Mater. Trans.* 52 (2021) 889–896, <https://doi.org/10.1007/s11661-021-06138-3>.
- [38] P. Sahu, A.S. Hamada, R.N. Ghosh, L.P. Karjalainen, X-Ray diffraction study on cooling-rate-induced γ fcc \rightarrow ϵ hcp martensitic transformation in cast-homogenized Fe-26Mn-0.14C austenitic steel, *Metall. Mater. Trans.* 38 (2007) 1991–2000, <https://doi.org/10.1007/s11661-007-9240-4>.
- [39] M. Hou, K. Li, X. Li, X. Zhang, S. Rui, Y. Wu, Z. Cai, Effects of pulsed magnetic fields of different intensities on dislocation density, residual stress, and hardness of Cr4Mo4V steel, *Crystals* 10 (2020) 115, <https://doi.org/10.3390/cryst10020115>.
- [40] S. Mitra, K.S. Arora, B. Bhattacharya, S.B. Singh, Effect of welding speed on the prediction accuracy of residual stress in laser welded 1.2 mm thick dual phase steel, *Lasers in Manufacturing and Materials Processing* 7 (2020) 74–87, <https://doi.org/10.1007/s40516-019-00107-w>.
- [41] Y. Liu, B. Wang, R. Liu, J. Guo, W. Shi, Effect of allotropic transformation on plasticity of Fe-15Mn-10Al-0.3C dual phase steel during annealing, *Cailiao Yanjiu Xuebao/Chinese Journal of Materials Research* 33 (2019) 837–847, <https://doi.org/10.11901/1005.3093.2019.136>.
- [42] P. Agrawal, R.S. Haridas, P. Agrawal, R.S. Mishra, Deformation based additive manufacturing of a metastable high entropy alloy via Additive friction stir deposition, *Addit. Manuf.* 60 (2022), 103282, <https://doi.org/10.1016/j.addma.2022.103282>.
- [43] Z. Li, C.C. Tasan, K.G. Pradeep, D. Raabe, A TRIP-assisted dual-phase high-entropy alloy: grain size and phase fraction effects on deformation behavior, *Acta Mater.* 131 (2017) 323–335, <https://doi.org/10.1016/j.actamat.2017.03.069>.
- [44] P. Niu, R. Li, Z. Fan, T. Yuan, Z. Zhang, Additive manufacturing of TRIP-assisted dual-phases Fe50Mn30Co10Cr10 high-entropy alloy: microstructure evolution, mechanical properties and deformation mechanisms, *Mater. Sci. Eng., A* 814 (2021), 141264, <https://doi.org/10.1016/j.msea.2021.141264>.
- [45] D. Wei, X. Li, J. Jiang, W. Heng, Y. Koizumi, W. Choi, B. Lee, H.S. Kim, H. Kato, A. Chiba, Novel Co-rich high performance twinning-induced plasticity (TWIP) and transformation-induced plasticity (TRIP) high-entropy alloys, *Scripta Mater.* 165 (2019) 39–43, <https://doi.org/10.1016/j.scriptamat.2019.02.018>.
- [46] P. Ramakrishnan, Welding metallurgy, *Indian Weld. J.* 4 (1972) 89, <https://doi.org/10.22486/iwj.v4i3.150243>.
- [47] S. Bhowmik, J. Zhang, S.C. Vogel, S.S. Nene, R.S. Mishra, B.A. McWilliams, M. Knezevic, Effects of plasticity-induced martensitic transformation and grain refinement on the evolution of microstructure and mechanical properties of a metastable high entropy alloy, *J. Alloys Compd.* 891 (2022), 161871, <https://doi.org/10.1016/j.jallcom.2021.161871>.
- [48] A. Kundu, S. Ghosh, R. Banerjee, S. Ghosh, B. Sanyal, New quaternary half-metallic ferromagnets with large Curie temperatures, *Sci. Rep.* 7 (2017) 1803, <https://doi.org/10.1038/s41598-017-01782-5>.
- [49] M. Koyama, H. Springer, S.V. Merzlikin, K. Tsuzaki, E. Akiyama, D. Raabe, Hydrogen embrittlement associated with strain localization in a precipitation-hardened Fe–Mn–Al–C light weight austenitic steel, *Int. J. Hydrogen Energy* 39 (2014) 4634–4646, <https://doi.org/10.1016/j.ijhydene.2013.12.171>.
- [50] K. Ichii, M. Koyama, C.C. Tasan, K. Tsuzaki, Localized plasticity and associated cracking in stable and metastable high-entropy alloys pre-charged with hydrogen, *Procedia Struct. Integr.* 13 (2018) 716–721, <https://doi.org/10.1016/j.prostr.2018.12.119>.